



Li₂B₄O₇:Mn for dosimetry applications: traps and mechanisms

Arno Ratas^a, Mikhail Danilkin^{a*}, Mihkel Kerikmäe^a, Aime Lust^a, Hugo Mändar^b,
Viktor Seeman^b, and Georg Slavin^c

^a Institute of Chemistry, University of Tartu, Ravila 14a, 50411 Tartu, Estonia

^b Institute of Physics, University of Tartu, Riia 142, 51014 Tartu, Estonia

^c Asper Biotech AS, Vaksali 17a, 50410 Tartu, Estonia

Received 23 September 2011, revised 1 June 2012, accepted 4 June 2012, available online 20 November 2012

Abstract. Thermoluminescence curves, kinetics, and Electron Paramagnetic Resonance (EPR) data were compared for Li₂B₄O₇:Mn and Li₂B₄O₇:Mn,Be radiation detectors. Analysis of the experimental data, both our own and published by other investigators, in connection with features of the crystal lattice structure allowed us to build models of traps and thermoluminescence mechanisms. The thermoluminescence peaks used in dosimetry are connected with the release of holes trapped at bridging oxygen near Mn²⁺ (or Be²⁺), substituting for tetrahedrally coordinated B³⁺. The luminescence occurs at Mn²⁺ substituting for Li⁺. Two types of Mn²⁺ centres give different luminescence and EPR spectra. The effects of Mn²⁺ interaction with surrounding oxygen atoms are discussed both for the Mn²⁺ luminescence band and for the hyperfine structure of EPR. Kinetics measurements revealed an additional “hopping” barrier for a hole to get to a recombination centre after it has been released from a trap. A simple kinetics model is suggested to describe the experimental data. The studies of optical stimulation spectra and optically stimulated emptying of traps demonstrated the possibility of using Li₂B₄O₇:Mn and Li₂B₄O₇:Mn,Be radiation detectors with optically stimulated readout systems.

Key words: physics of luminophors, chemistry of luminophors, luminescent dosimetry, lithium tetraborate, EPR of Mn²⁺.

INTRODUCTION

Solid-state luminescent dosimetry is based on radiation energy storage in dosimetric material in the form of lattice defects and captured charge carriers. The stored energy can be released as light at luminescence centres. Energy release is stimulated either by heating (thermally stimulated luminescence, TSL, TL) or by irradiating with light quanta of proper energy (optically stimulated luminescence, OSL). TL-based dosimeters are widely used in radiation dose monitoring. Both detectors themselves and equipped with detectors TL dosimeters are very compact and portable, but still require a readout system with a heating element, which is less compact compared with a system based on the OSL readout. OSL dosimetry systems can be really portable due to the application of light-emitting diodes.

LANDAUER® OSL dosimeters are based on Al₂O₃:C detectors, and their OSL dosimetric systems are probably the only ones that are widely known today on the market. On the one hand, crystalline corundum (Al₂O₃) detectors provide a high sensitivity and a low threshold of detectable radiation doses. On the other hand, the luminescence response of corundum to the radiation dose strongly depends on the energy of ionizing radiation in the region of tens to hundreds of keV. Corundum is not tissue-equivalent due to a higher effective atomic number compared with that of human tissue. As a result, the radiation dose from different radiation sources cannot be measured simultaneously (each separate case requires special calibration). The variation of response with radiation energy was studied for different detectors both experimentally [1–3] and by Monte-Carlo simulation [4]. The response of Li₂B₄O₇ demonstrates an almost energy-independent behaviour (fig. 1 in [4]), similar to the behaviour of water. The effective atomic number of

* Corresponding author, mikhail.danilkin@ut.ee

lithium tetraborate ($Z_{\text{eff}} = 7.39$) is very close to that of human tissue ($Z_{\text{eff}} = 7.42$). By tissue-equivalence, lithium tetraborate is one of the best among all known host materials for luminescence dosimetry. Hence, it would be a very attractive idea to try the OSL readout with radiation detectors based on lithium tetraborate. This explains the increased amount of efforts to study lithium tetraborate, both doped single crystals and $\text{Li}_2\text{B}_4\text{O}_7$ ceramic-based thermoluminescent detectors (TLDs).

Besides applications in luminescent dosimetry, $\text{Li}_2\text{B}_4\text{O}_7$ is studied also as an optical non-linear crystal [5]. The electronic structure of $\text{Li}_2\text{B}_4\text{O}_7$ has been also studied extensively, the previous calculations being refined and verified experimentally [6–10]. These studies elucidated the structure of energetic bands. $\text{Li}_2\text{B}_4\text{O}_7$ has a wide band gap (9 to 10 eV) and a structured valence band built up of three sub-bands. The valence band structure implies “heavy” and hardly mobilizable holes. This fact will be important for our further analysis of the features of TL kinetics and OSL.

Results of a comprehensive Electron Paramagnetic Resonance (EPR) and Electron Nuclear Double Resonance (ENDOR) study of the trapping centres in undoped $\text{Li}_2\text{B}_4\text{O}_7$ single crystals were published recently [11]. The samples with both natural and artificial isotopic composition were used for a better identification of hyperfine structures and models of paramagnetic centres. The Li vacancy was shown to stabilize a hole at the “bridging” oxygen (common vertex of two BO_4 tetrahedra). Electrons are trapped at boron ions near oxygen vacancies. The holes were shown to leave trapping centres at low temperatures: the corresponding paramagnetic centres do not survive above 90 K [11]. The high-temperature TSL is impossible without proper impurities.

To make a TLD material, $\text{Li}_2\text{B}_4\text{O}_7$ is usually doped with either Mn or Cu (or Ag). EPR and luminescence of $\text{Li}_2\text{B}_4\text{O}_7:\text{Cu}$ single crystals were studied recently [12–14]. Cu^{2+} was observed by EPR, while Cu^+ was detected by luminescence. The position of Cu^{2+} in the lattice of $\text{Li}_2\text{B}_4\text{O}_7$ was deduced from EPR. It has a low symmetry, and should be incorporated close to a regular Li^+ position but with distorted surroundings due to the displacement of large Cu^{2+} from a regular Li^+ site. As concerns Cu^+ , the luminescence studies demonstrated a stronger displacement but causally a higher local symmetry. EPR and optical studies of γ -irradiated $\text{Li}_2\text{B}_4\text{O}_7:\text{Mn}$, both single crystals and glass, have revealed different Mn centres [15]. The interpretation of obtained in [15] results is not so obvious, however. Also, the high radiation dose (50 kGy) given to the sample caused the recharging of Mn and essential radiation damage.

Radiation-induced absorption and photoluminescence were studied in $\text{Li}_2\text{B}_4\text{O}_7:\text{Mn}$ and $\text{Li}_2\text{B}_4\text{O}_7:\text{Ag}$ single crystals [16]. Very similar radiation-induced bands for $\text{Li}_2\text{B}_4\text{O}_7:\text{Mn}$ single crystals were observed also in [17].

The samples were given a radiation dose either of 12 kGy with a high-energy (4 MeV) electron beam [16] or a γ -radiation dose of 120 kGy [17]. Again, the applied dose was high enough to cause $\text{Mn}^{2+} \rightarrow \text{Mn}^{3+}$ transformation. Hence, some of the observed radiation-induced absorption bands were connected with manganese transformations at high doses and are not suitable for OSL readout in regular cases.

TSL (including luminescence spectral composition) was investigated for both $\text{Li}_2\text{B}_4\text{O}_7:\text{Mn}$ single crystals and glassy samples with different radiation doses and different amounts of added Mn in [18]. Reasonable X-ray doses of 1–60 Gy were used in this work. Two different but very close Mn^{2+} emissions (608 ± 2 and 598 ± 2 nm) were registered for different TSL maxima, with no dependence on the radiation dose. The TSL showed practically identical features for crystals with different amounts of manganese, but changed drastically in glass samples [18].

Our previous study [19] proved the decrease of the Mn^{2+} amount (estimated by EPR) at high radiation doses. At the same time, the amount of Mn^{2+} was found to be unchanged at doses up to 1–2 kGy. We studied also X-ray radiation-induced optical absorption and showed the decrease of the dosimetric TSL peak after optical stimulation at 365 nm [19]. This fact demonstrates a principal possibility of OSL readout for $\text{Li}_2\text{B}_4\text{O}_7$ -based detectors. Moving from a principal possibility to practical applications requires that several questions be answered. We are going to deal with two of them: What is the storage mechanism of excitation energy in $\text{Li}_2\text{B}_4\text{O}_7:\text{Mn}$? How can the OSL readout efficiency be improved? The first question was discussed in our previous paper [19], and will be considered again. As concerns the improvement of readout, we have tried to modify $\text{Li}_2\text{B}_4\text{O}_7:\text{Mn}$ by doping it with beryllium (patent pending [20]). This modification has opened new approaches, and also initiated the next round of investigations.

The present work compares EPR, TSL, kinetics, radiation-induced absorption, and OSL stimulation spectra in $\text{Li}_2\text{B}_4\text{O}_7:\text{Mn}$ and $\text{Li}_2\text{B}_4\text{O}_7:\text{Mn,Be}$. Comparative studies help to apprehend the nature of traps and energy storage mechanisms in these materials.

MATERIALS AND METHODS

Ceramic samples of $\text{Li}_2\text{B}_4\text{O}_7:\text{Mn}$ and $\text{Li}_2\text{B}_4\text{O}_7:\text{Mn,Be}$ were used. According to X-Ray Powder Diffraction (XRPD), the samples contain a well-formed crystalline phase. Small crystals are bound together with a glassy phase. The amount of the binding glassy phase, however, is very small compared to the amount of polycrystalline material. The initial lithium tetraborate was obtained by the following reaction:



The typical Mn concentration was 0.13–0.26 mol%. The concentration of Be was either the same or twice the Mn amount. Manganese carbonate was added at the stage of initial synthesis in water suspension at continuous stirring and heating the mixture. In case of Li₂B₄O₇:Mn,Be samples, BeO was added at the same moment as manganese. The water was evaporated, and then the residual water and CO₂ were removed by heating at 823 K for 120 min under flowing nitrogen. Then, the luminophor was ground in a mortar, and tablets were pressed. The sets of tablets were sintered at different temperatures (1133–1213 K). Most data were obtained with samples sintered at the temperature close to the melting point of lithium tetraborate (1190 K).

The XRPD pattern was obtained using a computer-controlled Bragg–Brentano Θ-2Θ powder diffractometer (equipped with a goniometer GUR-5 from diffractometer DRON-1). The samples were irradiated either with a first-class ²³⁹Pu radiation source (6.02×10^5 α-particles per second, dose rate about 1.23 mGy s⁻¹ for a 4.5-mm tablet) or by means of an X-ray tube with a tungsten anode (53 kV, 15 mA, dose rate about 32 Gy s⁻¹ cm⁻²). A ⁹⁰Sr/⁹⁰Y radiation source 6527B (Sweden, about 3 mGy per rotation) was used as well.

The TL curves and kinetics were measured with a home-made TL reader based on computer-driven thermocontroller OMRON E5CK and PMT FEU-79 equipped with a current-to-frequency converter. The measured data were automatically collected and stored at a data server. Statistical refinement and pre-treatment of data were carried out by a special computer program, written for this particular installation.

The decay curves (kinetics) were measured after excitation with α-particles (600–6000 s for Li₂B₄O₇:Mn and 600–3600 s for Li₂B₄O₇:Mn,Be). The measurements were performed after cleaning the low-temperature peaks (pre-heating for 100 s at 395 K for Li₂B₄O₇:Mn and 240 s at 464 K for Li₂B₄O₇:Mn,Be). After pre-heating, the sample was removed from the heater surface. Then the heater temperature was increased to the desired value, and only after that the sample was placed back onto the heater to measure decay kinetics. The data collected before the thermal equilibrium was achieved were not used in further analysis. This technique is applicable when the non-equilibrium state lasts less than the time-constant of the fastest decay, and the total time of measurements exceeds 4–5 times the time-constant of the slowest decay.

The spectral composition of thermoluminescence peaks was measured with an optical spectrometer Newport OSM2-100DUV. The spectrometer is equipped with an optical wave-guide. The spectrum in the selected range was recorded with a CCD array for a known period of time (up to 1 min). The data were

transferred to a computer and corrected for spectral and amplitude sensitivity of CCD elements. During the measurements the sample was kept at a temperature of about 660–680 K using an electric heater.

The optical depopulation of traps was studied at two different wavelengths using two powerful LEDs: HEXAGON H2A1-H365 (peak of emission at 365 nm, 25 mW of light power) and HEXAGON H2A1-H395 (395 nm, 95 mW).

The OSL spectra were measured using a 1000 W Xenon-arc lamp combined with a Zeiss SPM-2 monochromator. The integrated emission was measured by PMT (FEU-39) with a quartz window. Two shutters were installed to separate the excitation and measuring periods of time: the first one at the entrance of the monochromator and the second one in front of the PMT. The latter opens automatically 0.05 s after the first shutter has been closed. The “dark” pause of 0.05 s was selected to separate the stimulated recombination luminescence from the directly excited one (intra-centre processes have a decay time of 10^{-5} – 10^{-8} s).

Radiation-induced optical absorption bands were obtained by measuring diffuse reflectance spectra before and after X-irradiation. The spectra were recorded at least twice, then averaged. Absorption bands were extracted by dividing the spectrum of the X-irradiated sample by the spectrum measured before X-irradiation. The measurements were performed with a computer-driven monochromator MChD-2 (LUMEX, Russia), equipped with a PMT HAMAMATSU R7400U-04, pre-amplifier, and voltmeter with a computer-driven data acquisition system. The halogen incandescent lamp Narva 55133 HLWS5 was used as the light source. It was powered by a regulated-voltage stabilized source. The lamp was forced up to 28 W to obtain more light in the UV region.

The EPR measurements were performed both at room temperature and at liquid nitrogen temperature. An X-band (9.1 GHz) spectrometer with a 975 kHz magnetic field modulation was used.

RESULTS AND DISCUSSION

Material characterization and features of the crystal structure

The results of XRPD analysis are shown in Fig. 1. The finished detectors (tablets) demonstrate a very distinct pattern corresponding to Li₂B₄O₇. The shapeless background of glassy phases is not seen for sintered tablets. There are no effects from either Mn or Be doping: the concentration of added impurities is too low (about one impurity atom per hundred lattice units), so the XRPD pattern shows neither pronounced distortions nor separate phases. The insertions in Fig. 1 show the improvement of the Li₂B₄O₇ crystal lattice in tablets

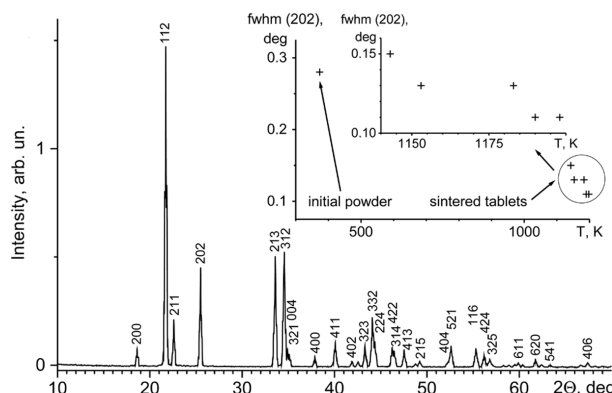


Fig. 1. XRPD pattern for a sintered tablet (1198 K) corresponds to $\text{Li}_2\text{B}_4\text{O}_7$, whose characteristic reflexes are marked. The insertions demonstrate how the lattice structure improves with sintering temperature increase. Lattice improvement can be assessed by the decrease of the 202 reflex line width (fwhm).

with increasing sintering temperature. The lower insertion shows a very pronounced improvement of lattice

structure in sintered tablets compared to the raw material, while the upper insertion demonstrates a further improvement taking place up to the melting point of $\text{Li}_2\text{B}_4\text{O}_7$. The effect is followed by the decrease of the full-width-half-maximum (fwhm) parameter of the line of the most separated reflex 202.

Lithium tetraborate has a tetragonal body centred unit cell with cell parameters $a = 0.9475 \text{ nm}$ and $c = 1.0283 \text{ nm}$ [21]. There are eight formula units ($\text{Li}_2\text{B}_4\text{O}_7$) in the unit cell and seven atoms in the asymmetric unit: one lithium (Li), two different borons (B1 and B2), and four oxygen atoms (O1, O2, O3, and O4). The space group I41cd generates a total of 104 atoms in one unit cell: 16 Li, 16 B1, 16 B2, 16 O1, 16 O2, 16 O3, and 8 O4. By looking at the B–O coordination, two types of polyhedral structure elements can be distinguished in the structure: triangles and tetrahedra. All B1 belong to triangles (coordinated by O1, O2, and O3), and all B2 are tetrahedrally coordinated with oxygen atoms. The bridging oxygen between two B + 4O groups is always O4. The lattice structure of lithium tetraborate is illustrated in Fig. 2. The illustration is created using the Balls & Sticks computer program [22].

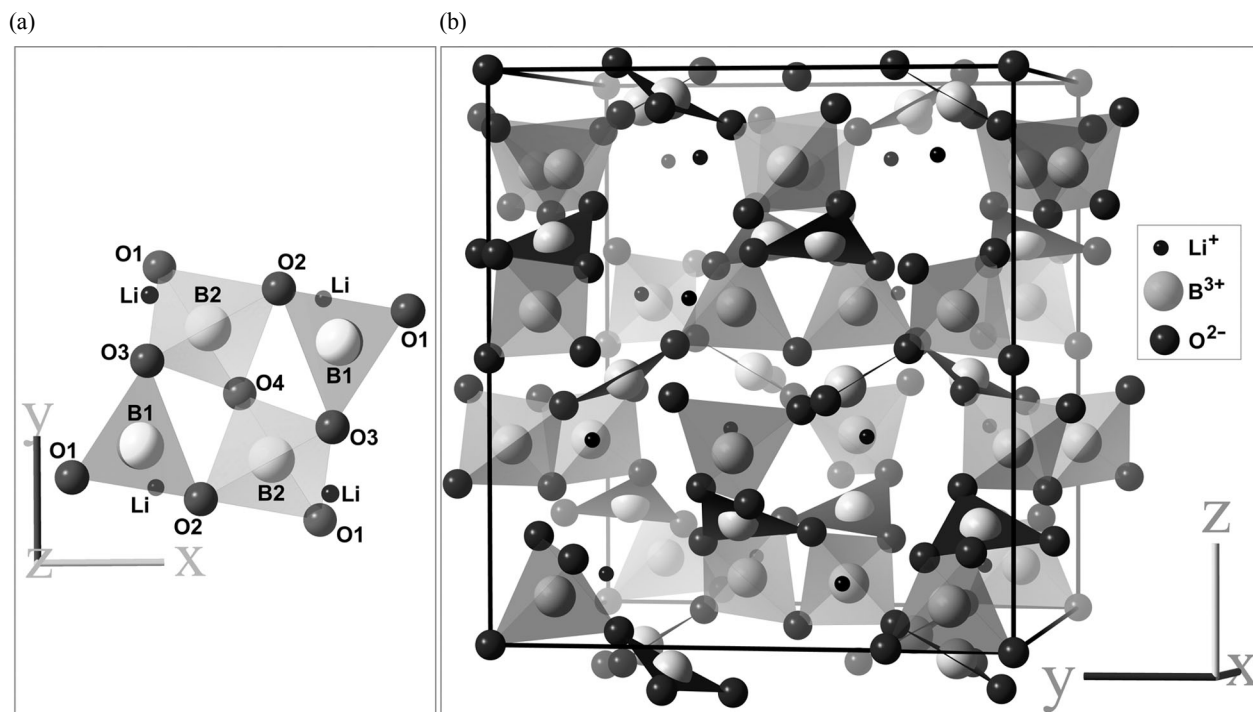


Fig. 2. (a) Main crystal motif of lithium tetraborate consisting of two basic elements: two identical planar trigonal ($\text{B}_1 + \text{O}_1 + \text{O}_2 + \text{O}_3$) and two identical tetrahedral ($\text{B}_2 + \text{O}_1 + \text{O}_2 + \text{O}_3 + \text{O}_4$) groups. Tetrahedral groups have a common vertex O_4 and are joined additionally by planar boron–oxygen triangles. Li ions are located in the interstices of the boron–oxygen framework. (b) Balls & sticks model of lithium tetraborate lattice. A unit cell is outlined with a solid-line parallelepiped. Basic elements ($\text{B} + 4\text{O}$ tetrahedra and $\text{B} + 3\text{O}$ triangles) are marked with semi-transparent planes. Sizes of balls are not in scale with ionic radii of atoms.

It is common to describe the main crystal motif (Fig. 2a) of lithium tetraborate as a boron–oxygen complex ($4\text{B} + 9\text{O}$), consisting of two identical planar trigonal ($\text{B} + 3\text{O}$) and two identical tetrahedral ($\text{B} + 4\text{O}$) groups. There are a total of eight boron–oxygen complexes in the unit cell. The lithium ions stabilize the boron–oxygen framework being distributed in helicoidal voids spreading along the z -axis.

All tetrahedral groups are considered to be identical, which is obviously true for the perfect crystal. In the presence of either intrinsic or impurity defects, a difference appears between initially equivalent units. For example, EPR and ENDOR studies of a hole captured at “bridging oxygen” (O_4 in Fig. 2a) demonstrate that it “has nearly equal hyperfine interactions with two adjacent boron nuclei” [11]. However, two very close sets of lines were distinguished. The small difference between the two initially equal B_2O_4 distances observed in [11] can be explained by the presence of a Li vacancy near one of the two adjacent tetrahedral units. It causes either deformation of one of the two adjacent tetrahedra or their orientation displacement.

Lithium sites and space in helicoidal voids are regarded usually as the only possible places to be occupied by various impurities in lithium tetraborate. This comes from the comparison of ionic radii of different impurities with the sizes of possible sites in the $\text{Li}_2\text{B}_4\text{O}_7$ lattice. For example, Mn^{2+} in tetrahedral coordination (80 pm, http://webelements.com/manganese/atom_sizes.html (visited 23.09.2012)) is drastically larger than B^{3+} in tetrahedral coordination (25 pm,

http://webelements.com/boron/atom_sizes.html (visited 23.09.2012)). That is why a substitution of B^{3+} with Mn^{2+} seems to be hardly possible. Nevertheless, we shall regard below the possibility of such substitution in order to explain some experimental data. Hence, we need some closer consideration of the question. The lengths of $(\text{B}^{3+}\text{--O}^{2-})$, $(\text{Mn}^{2+}\text{--O}^{2-})$, $(\text{Mn}^{3+}\text{--O}^{2-})$, and $(\text{Be}^{2+}\text{--O}^{2-})$ bonds in some substances are compared in Table 1. The distances $(\text{B}^{3+}\text{--O}^{2-})$ in lithium tetraborate tetrahedra vary from 145.0 to 150.5 pm. The distances $(\text{Mn}^{2+}\text{--O}^{2-})$ usually exceed 200 pm in manganese–boron oxides, while the $(\text{Mn}^{3+}\text{--O}^{2-})$ distances are shorter. Hence, if manganese incorporation at tetrahedral boron sites is still possible in lithium tetraborate, this should occur much more easily for Mn^{3+} than for Mn^{2+} (there is also no need to compensate for a charge). Incorporation of manganese in a very tight tetrahedral environment is proved by EPR in BeO ceramics with the wurtzite crystal structure [27]. Mn^{2+} occupies Be^{2+} sites of tetrahedral symmetry in BeO despite short rigid covalent bonds in this substance. Oxygen tetrahedra in $\text{Li}_2\text{B}_4\text{O}_7$ are less rigid compared to the BeO lattice. The B_2O_4 bond (Fig. 2a) is the weakest one in $\text{Li}_2\text{B}_4\text{O}_7$ [28] and has the most pronounced variations of the length with temperature [21]. If either Mn^{3+} or Mn^{2+} occurred at the position of B_2 , the tetrahedron size could be increased mostly on the account of a weak bond with the O_4 atom. So, the incorporation of manganese into lithium tetraborate at Li positions seems to be possible without doubt, and probably possible at B_2 positions, too. We shall recall these ideas in the next sections.

Table 1. Manganese–oxygen bond lengths in some substances

Structure and elements	Bond length, pm	Substances and references
$\text{Mn}^{2+}\text{--O}^{2-}$ (4 closest O^{2-})	209.2–214.1	Manganese diborate MnB_4O_7 [23], orthorhombic
$\text{Mn}^{2+}\text{--O}^{2-}$ (distorted octahedral)	202–228	Jimboite $\text{Mn}_3(\text{BO}_3)_2$ [24]
$\text{Mn}^{2+}\text{--O}^{2-}$ (distorted octahedral)	208.6–224.7	Manganese(II,III) oxyborate Mn_2OBO_3 [25], monoclinic
$\text{Mn}^{3+}\text{--O}^{2-}$ (distorted octahedral)	188.1–197.7	Manganese(II,III) oxyborate Mn_2OBO_3 [25], monoclinic
$\text{Be}^{2+}\text{--O}^{2-}$ (tetrahedral)	168.5–168.6	Beryllium oxide BeO [26], wurtzite Mn^{2+} detected at Be^{2+} positions by EPR [27]
$(\text{B}^{3+} + 4\text{O})$ tetrahedra		Lithium tetraborate $\text{Li}_2\text{B}_4\text{O}_7$ [21] (Fig. 2)
$\text{B}_2\text{--O}1$	145.0	
$\text{B}_2\text{--O}4$	145.3	
$\text{B}_2\text{--O}3$	150.2	
$\text{B}_2\text{--O}2$	150.5	
Li–O bonds		Lithium tetraborate $\text{Li}_2\text{B}_4\text{O}_7$ [21] (Fig. 2)
$\text{Li}\text{--O}1$	218.1	
$\text{Li}\text{--O}2$	197.0	
$\text{Li}\text{--O}3$	203.5	
$\text{Li}\text{--O}3'$	207.0	
$\text{Li}\text{--O}4$	259.2	

Thermoluminescence and its spectral composition

The TSL curves of $\text{Li}_2\text{B}_4\text{O}_7:\text{Mn}$ (a1)–(a2) and $\text{Li}_2\text{B}_4\text{O}_7:\text{Mn,Be}$ (b1)–(b2) are shown in Fig. 3. $\text{Li}_2\text{B}_4\text{O}_7:\text{Mn}$ demonstrates two groups of TSL maxima. The first one, a low-temperature (335–345 K) peak, decays very soon after excitation, so it cannot be used for dosimetry. The second group of TSL maxima (470–510 K), which is stable for a long period of time (several months or even years), is used in dosimetry. The TSL curve of $\text{Li}_2\text{B}_4\text{O}_7:\text{Mn}$ demonstrates no essential differences from previously reported cases, either for TL detectors [19] or for single crystals [18,28]. It is essential to note that the two groups of TSL maxima have different spectral composition of luminescence. We observed the difference by naked eye, and then tried to record the spectra. The spectra of peaks (a1) and (a2) are shown in the insertion of Fig. 3.

As the used installation was insufficiently sensitive, the recorded spectra are not enough demonstrative. So, we refer here to more accurate data from [18]. The low-temperature (335–345 K) TSL has a red luminescence band with a maximum at 608 ± 2 nm, while the high-temperature (470–510 K) TSL has an orange band with a maximum at 598 ± 2 nm [18]. Both luminescence bands can be attributed to ${}^4\text{T}_1 - {}^6\text{A}_1$ radiative transitions of Mn^{2+} in distorted tetrahedral environments. There should be two different cases, with Mn^{2+} occupying different sites in the lattice of $\text{Li}_2\text{B}_4\text{O}_7$. The possibility for Mn^{2+} to occupy B^{3+} tetrahedral position (B2) was discussed in the previous section, and some additional evidence will be given later.

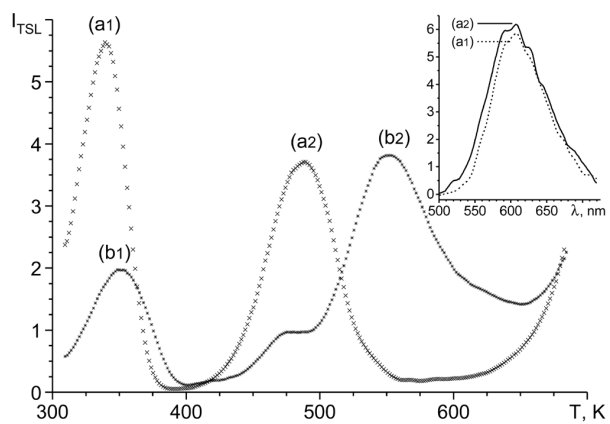


Fig. 3. TSL curves for $\text{Li}_2\text{B}_4\text{O}_7:\text{Mn}$ (a1)–(a2) and $\text{Li}_2\text{B}_4\text{O}_7:\text{Mn,Be}$ (b1)–(b2). The samples were excited for 100 s with ${}^{239}\text{Pu}$ radiation source; then TSL was measured after a pause of 100 s (to keep the same conditions for the rapidly decaying first peak). The heating rate was 0.37 K s^{-1} . The thermal background produced by the heater (above 625 K) is not subtracted. The insertion illustrates the difference in the spectral composition of peaks (a1) and (a2) for $\text{Li}_2\text{B}_4\text{O}_7:\text{Mn}$.

Let us consider now the Li^+ environment. The Li atoms are surrounded by O1, O2, O3, and O3' (the first coordination sphere). The distances to these four oxygen atoms are not equal and vary from 197.0 to 218.1 pm. Hence, the closest coordination of Li is a distorted tetrahedron, where Li is displaced from the centre in the direction of the O4 atom (Li–O4 distance is 259.2 pm). This atom can be considered as the fifth top of the Li–O polyhedron [21]. Hence, if Mn^{2+} occupied any of the two positions, either of Li or of B2, in both cases it would occur in a distorted tetrahedral field of oxygen ligands. The tetrahedron of $\text{B} + 4\text{O}$ is smaller than the tetrahedron of $\text{Li} + 4\text{O}$ (Table 1). This implies a stronger field of oxygen ligands when Mn^{2+} occupies the tetrahedral position of B^{3+} .

The electronic clouds of the d-electrons of Mn^{2+} overlap with clouds of the valence electrons of oxygen ligands. The larger overlap produces stronger screening between the d-electrons and hence a larger reduction of the Racah parameters, resulting in a decrease in luminescence energy [29]. Hence, the Mn^{2+} at the B^{3+} tetrahedral position could have the luminescence band at lower energy than that of Mn^{2+} at the Li^+ site. The luminescence bands of both types of Mn^{2+} are observed in the orange–red region. A tetrahedral Mn^{2+} is usually thought to have mostly green–yellow luminescence contrary to Mn^{2+} in the octahedral symmetry where a stronger field causes an orange–red luminescence band. However, this idea should not be taken as a “universal approach”, especially for distorted tetrahedral sites. Two excited levels E and T are valid for pure tetrahedral symmetry. A strong low-symmetry field of ligands (arranged as a distorted and very tight tetrahedral environment) causes an additional splitting of these levels. This results in an additional shifting of the first excited state to lower energy, thus decreasing the energy of radiative transition [30]. Hence, the red luminescence band (608 ± 2 nm [18]) should be attributed to the Mn^{2+} in the tighter oxygen environment (probably, at the B^{3+} tetrahedral site), while the orange band (598 ± 2 nm [18]) should belong to the Mn^{2+} with a looser oxygen environment (most probably, at the Li^+ site).

If the idea of Mn^{2+} substitution for B^{3+} in $\text{B} + 4\text{O}$ tetrahedra is true, the weak bond of the O4 atom with two tetrahedra should become even weaker, and O4 would become a hole trap. Recombination at this trap should give red luminescence, while the orange luminescence band at higher temperatures should be caused by a recombination of released holes at some electron trap near Mn^{2+} at the Li^+ site (where the oxygen environment is not so tight). We shall return to the discussion of TSL mechanisms later, after disclosing some evidence of two different Mn^{2+} centres obtained by EPR.

In case of $\text{Li}_2\text{B}_4\text{O}_7:\text{Mn,Be}$ (see Fig. 3, curve (b1–b2)), the TSL peak at 470–510 K is essentially suppressed in

favour of a new intensive group of maxima created in the range of 525–625 K (b2). Smaller Be^{2+} would occupy the positions of tetrahedral B^{3+} much more efficiently than Mn^{2+} . This would cause the amount of Mn^{2+} at the position of B^{3+} to decrease, and the amount of Mn^{2+} at the position of Li^+ to increase. We shall see below the correspondence of this supposition with our EPR data. Small Be^{2+} at the B^{3+} position would distort the oxygen tetrahedron much less than Mn^{2+} , with O4 being displaced towards positive Li^+ to a much lesser extent. Hence, the hole trap at O4 near Be^{2+} substituting for B^{3+} would be deeper than in case of Mn^{2+} . Indeed, the observed for $\text{Li}_2\text{B}_4\text{O}_7:\text{Mn,Be}$ high-temperature TSL peak (525–625 K, see Fig. 3, (b2)) occurs at a higher temperature than for $\text{Li}_2\text{B}_4\text{O}_7:\text{Mn}$, while the low-temperature peak (470–510 K, Fig. 3, (a2)) is essentially suppressed.

EPR of Mn^{2+} in $\text{Li}_2\text{B}_4\text{O}_7:\text{Mn}$ and $\text{Li}_2\text{B}_4\text{O}_7:\text{Mn,Be}$

The studies of EPR spectra of Mn^{2+} ions in lithium borate glasses and compounds have a long history [15,31–36]. With the X-band EPR techniques, the EPR lines at low magnetic fields were observed, formally corresponding to $g \approx 4.3$ and $g \approx 3.3$. These lines are often attributed to centres with different local symmetry features [15,33–36]. A reasonable explanation is suggested in [31]. When using a 35 GHz spectrometer instead of a 9.4 GHz one, the authors have observed that the centre of the Mn^{2+} principal hyperfine sextet appears only at the position of $g \approx 2.0$. The result was interpreted by assuming a spin-Hamiltonian containing crystal field terms comparable to the Zeeman energy at the X-band [31]. A strong crystal field in lithium borate systems (including glasses) is expected at the distorted tetrahedral sites, both at the Li^+ and B^{3+} positions, either in the crystal lattice or in the glass network. The strong crystal field in the local surrounding of Mn^{2+} causes the EPR lines to be distributed in a very wide range of magnetic fields in the X-band EPR spectra. This is true for various complex oxide systems and glasses. We refer here to the EPR study of Mn^{2+} in $70\text{TeO}_2 \cdot 25\text{B}_2\text{O}_3 \cdot 5\text{MO}$ (MO is either SrO or SrF_2) [34], where the boron-oxide structure is not a glass former. The authors use the Mn^{2+} hyperfine splitting (HFS) value to estimate the extent to which the bonds between Mn^{2+} and the surrounding atoms are covalent [34]. Another interesting result of [34] concerns the clusterization of Mn^{2+} and the formation of a strong broad line in the region of $g \approx 2.0$.

Our EPR spectra of $\text{Li}_2\text{B}_4\text{O}_7:\text{Mn}$ and $\text{Li}_2\text{B}_4\text{O}_7:\text{Mn,Be}$ are shown in Fig. 4a and 4b, respectively. A very intensive narrow line near 0.325 T is connected with the large radiation dose. This line disappeared after annealing the sample at 700 K for 90 min, and it did not appear again after X-irradiation with a dose of

≈ 1000 Gy. We shall not discuss the nature of this radiation-induced EPR defect in this paper.

Two different Mn^{2+} centres were already mentioned in our previous paper [19]. We shall analyse here some additional information. First, there are substantial differences between the spectra recorded at room temperature (RT) and at liquid nitrogen temperature (LNT) (see Fig. 4). The LNT spectrum of $\text{Li}_2\text{B}_4\text{O}_7:\text{Mn}$ (Fig. 4a, LNT) contains several groups of lines. The sextets near 0.25 T and also mutually overlapped sextets near 0.35 T are hyperfine structures (HFS) of Mn^{2+} . The spectrum in the region of 0.15 T contains several superimposed Mn^{2+} HFS lines belonging to different centres. At room temperature, the spectrum of another type of Mn^{2+} centres is dominating, with a different fine structure and larger HFS splitting. These obvious differences in the spectra of Mn^{2+} centres should be interpreted in terms of different interaction of Mn^{2+} with ligands. The stronger interaction of d-electrons of Mn^{2+}

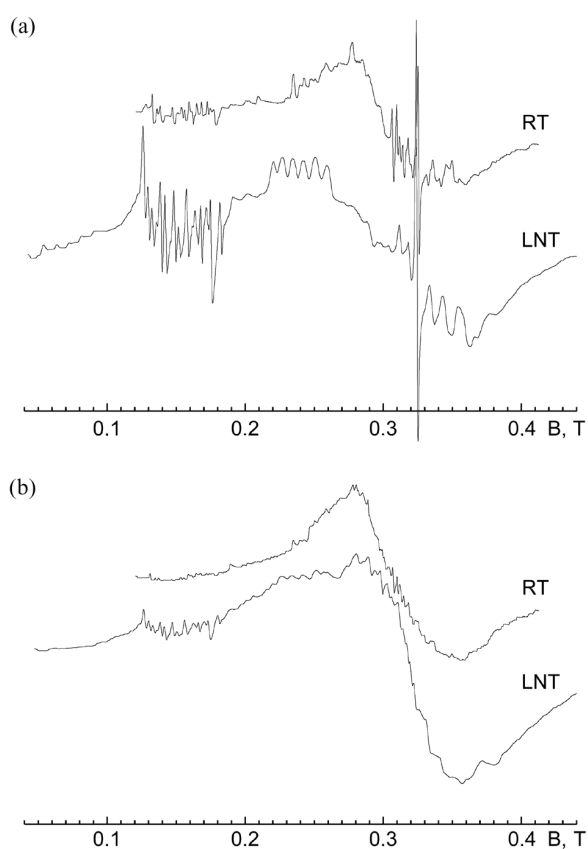


Fig. 4. EPR spectra of $\text{Li}_2\text{B}_4\text{O}_7:\text{Mn}$ (a) and $\text{Li}_2\text{B}_4\text{O}_7:\text{Mn,Be}$ (b) measured at room temperature (RT, upper spectra) and at liquid nitrogen temperature 77 K (LNT, lower spectra). The background signals of the empty quartz Dewar flask and empty sample holder have been subtracted. The spectra were recorded under the same conditions (field modulation amplitude, microwave power) and are shown in the same scale.

with p-electrons of oxygen ligands causes the stronger polarization effects in inner s-orbitals, and hence, a lower splitting in HFS [34]. The Mn²⁺ centres possessing stronger (more covalent) bonds with the surrounding oxygen atoms give dominating spectra at LNT. The average distance between HFS lines in the region of 0.22–0.26 T is ≈ 8.4 mT. It is interesting to note that the HFS of these centres is close to the splitting observed in [27] for Mn²⁺ in BeO (about 8.2 mT). Mn²⁺ at the B³⁺ position in Li₂B₄O₇:Mn would be surrounded with tetrahedrally coordinated oxygen atoms but with a lower symmetry than in BeO. However, the HFS splitting is similar due to the similarity of Mn–O distances in these two cases. The larger HFS splitting (about 9–9.5 mT) corresponds to Mn²⁺ at the Li⁺ position. There are larger Mn–O distances and less covalent bonds in this case, and also, the temperature dependence of the EPR signal is less pronounced.

The two different luminescence bands observed in Li₂B₄O₇:Mn [18] are also connected with the different interaction of Mn²⁺ with ligands in different surroundings (see text above). Here we have a good correlation of EPR and luminescence data. However, detailed analysis of the spectrum in the region of 0.30–0.38 T would be a complex task due to the superimposed hyperfine structures from different centres. The same difficulties are encountered in the region of 0.12–0.19 T, where several different HFS structures overlap each other.

We measured also the EPR spectra of samples containing a fourfold higher Mn amount. The amount of Mn²⁺ with the lower HFS splitting (at the B³⁺ position) increased only 1.5–2 times. The same was true for the intensity of the main TSL peak. Here we have once again a good correlation of EPR and TSL data. The increase of the Mn amount caused mostly a wide line to increase in the region of 0.28–0.37 T. This behaviour of Mn²⁺ is analogous to that observed in [34] due to clusterization effects.

The HFS lines of Mn²⁺ are essentially suppressed in Li₂B₄O₇:Mn,Be (Fig. 4b). The figure shows the case when equal amounts of Be and Mn were added, and Mn²⁺ HFS lines are still more suppressed with the amount of Be being twice the amount of Mn. While the HFS of Mn²⁺ almost disappeared, the wide line in the region of 0.28–0.37 T was the only one that increased. The results can be explained by the suppression of the incorporation of Mn²⁺ into B³⁺ positions (Be²⁺ takes these positions much more easily), with the simultaneous increase of Mn clusterization effects in the voids of the Li₂B₄O₇ lattice structure. These results are in good correlation with TSL data: a TL peak connected with Mn is suppressed by Be, and a new TL peak appears instead at higher temperatures.

Let us recall the correlation of TSL intensity and the amount of Mn²⁺ detected by EPR in our previous study [19]. The amount of each of the two types of Mn²⁺

centres correlates with the dosimetric TSL peak intensity. We suggest the following explanation of the obtained result. At low temperature stages of synthesis (during the reaction in water and pre-heating at 823 K), Mn could substitute for B³⁺ as Mn³⁺ without any charge compensation required. This would cause still smaller distortions of the oxygen tetrahedron. When tablets are sintered at elevated temperatures, Mn³⁺ is reduced to Mn²⁺, and then the tetrahedra containing Mn²⁺ are partially destroyed. The destroyed part is exactly the one required for charge compensation: the released Mn²⁺ occupies the Li⁺ position somewhere in the vicinity of the Mn²⁺ that remains at the B³⁺ position. This explains the simultaneous increase of the amounts of both Mn²⁺ types with increasing sintering temperature (as it was observed by EPR in [19]). The idea of Mn_B–Mn_{Li} charge-compensating pairs is indirectly supported by strong exchange interactions observed with SQUID-magnetometer for X-ray excited samples (this material will be published separately). This kind of charge-compensation mechanism does not require Li vacancies to compensate for Mn²⁺ at the Li⁺ position.

The idea of initial incorporation of manganese in the form of Mn³⁺ is indirectly supported also by some chemical experiments. For example, Li₂B₄O₇:Mn with the same TL properties was successfully obtained using KMnO₄ instead of MnCO₃. This fact demonstrates that the oxidation state of manganese is governed by the technological process itself and not by starting materials. After all, the idea of Mn³⁺ incorporation at the position of B³⁺ with further transformation into Mn²⁺ during the sintering process appears to be quite reasonable.

Thermoluminescence mechanisms and traps

Before we begin, let us exclude the possibility of Mn³⁺–Mn²⁺ transformations and the resulting luminescence of Mn²⁺. We speak here about relatively moderate doses (not exceeding 2000–3000 Gy) at which no Mn transformations were detected by EPR [19].

The EPR data and spectral composition of TL peaks give an initial guess for the nature of TL peaks. The low-temperature (335–345 K) peak yields a red luminescence band centred at 608 ± 2 nm. This luminescence band should come from Mn²⁺ at the position of tetrahedral B³⁺. We suppose a hole to be trapped at O4 near this Mn²⁺. A hole trapped at O4 was studied by EPR and ENDOR [11], but in the studied case it was stabilized by Li vacancy and had a low thermal stability (only up to 90 K). When Mn²⁺ substitutes for B³⁺, the lack of positive charge at the B³⁺ position produces a much deeper hole trap at O4 oxygen. The hole trapped here causes a bond between two tetrahedra to get practically broken. Thermal stabilities of hole centres at broken oxygen bonds were shown to be very high in borate glasses [37]. The red luminescence band of Mn²⁺ at the position of tetrahedral

B^{3+} is excited when captured at O4 hole undergoes recombination with some electron. So, the low-temperature TSL peak is caused by the recombination directly at the site where a hole is trapped. Oxygen O4 should efficiently transfer the recombination energy to the Mn^{2+} at the position of tetrahedral B^{3+} . We shall discuss the nature and mechanism of these processes later.

Let us turn now to the next TSL peak (470–510 K). It shows an orange luminescence band (centred at 598 ± 2 nm) and should be connected with Mn^{2+} at the Li^+ position. This peak is used in dosimetry; its intensity correlates with the amount of Mn^{2+} observed by EPR [19]. It should be caused by a recombination of released holes with electrons captured near Mn^{2+} at the Li^+ position. We suppose that the holes are released from O4 near Mn^{2+} substituting for B^{3+} . The traps responsible for this peak were destroyed after the sample was annealed in vacuum [28] due to the loss of O4, as the authors of [28] concluded. We agree with this idea and say more in its favour: O4 has still a weaker bonding when one of the two tetrahedral B^{3+} is substituted with Mn^{2+} . Once O4 is removed, the corresponding Mn^{2+} can be also released from the position of B^{3+} , making the destruction of some part of hole traps irreversible. Exactly this effect was observed in experiments in [28]. Moreover, the amount of Mn^{2+} at the position of Li^+ increased after all annealing steps, thus giving a dominating orange band in radioluminescence [28].

Let us turn back to the TSL peak at 470–510 K in $\text{Li}_2\text{B}_4\text{O}_7:\text{Mn}$ with no Be added. A hole released from O4 near Mn^{2+} at the B^{3+} position would cause the luminescence of Mn^{2+} substituting for Li^+ only if there is some electron trapped near this Mn^{2+} . Otherwise, neither a hole would be delivered against a repelling Coulomb force nor a recombination would occur. The orange luminescence band (centred at 598 ± 2 nm) of Mn^{2+} can be observed if the recombination energy is efficiently transformed into the excited state of Mn^{2+} at the Li^+ position.

Let us see how these two “ifs” could be realized. The first “if”: What kind of an electron trap can exist in the vicinity of Mn^{2+} at the Li^+ position? The Li^+ ions in the $\text{Li}_2\text{B}_4\text{O}_7$ lattice are placed as spaced pairs in helicoidal voids of the boron-oxide frame (see Fig. 2b). Hence, when Mn^{2+} substitutes for Li^+ , the repelling Coulomb force is expected to shift the other closest Li^+ out from its regular position. Li would be probably moved to the closest interstitial position described in [38] in connection with mechanisms of ionic conductivity in $\text{Li}_2\text{B}_4\text{O}_7$. The closest interstitial position for Li is situated at about 61 pm over the face of the oxygen polyhedron surrounding the regular Li site [38]. The extra positive charges of both Mn^{2+} and displaced Li^+ would split off the trapping level from the bottom of the

conduction band. The states at the conduction band minimum are built of the antibonding BO_3 -orbitals [9]. In our case, a BO_3 group would be close to both Mn^{2+} and the displaced Li^+ . We cannot speculate about the detailed structure of the electron trap, but some overlap of the Mn^{2+} excited state with the wave function of a trapped electron seems to be very probable. This facilitates the transfer of the recombination energy to Mn^{2+} and removes the second “if” in our model. The details of the structure of this electron trap could be studied by EPR, and this work is yet to be done.

However, we refer here to some electron traps observed by EPR in neutron-irradiated $\text{Li}_2\text{B}_4\text{O}_7$ with different isotope compositions [39]. The authors called these paramagnetic centres “ Li^0 centres”. The hyperfine structure in the EPR spectra of paramagnetic defects was surely caused either by ${}^6\text{Li}$ or ${}^7\text{Li}$ nuclei. However, the reported splitting constant A value (about 1 mT) is too small compared with the cases when the wave function of the electron is located mostly on Li. For example, EPR of Li^0 deposited at the surface of MgO gives a value of 7.4 mT for hyperfine splitting [40]. Hence, the observed in $\text{Li}_2\text{B}_4\text{O}_7$ EPR signals associated with Li^0 in [39] should be related rather to an electron located somewhere in the vicinity of Li, with the wave function of the electron overlapping the Li nucleus only partially. This case would be realized if the electron belonged mostly to some ligands in the vicinity of Li; probably, when Li is displaced to an interstitial position due to neutron irradiation. This seems to be very similar to our idea of an electron trap in $\text{Li}_2\text{B}_4\text{O}_7:\text{Mn}$. So, we have probably a good initial guess for the future EPR studies.

The electron trap at BO_3 near positively charged Mn^{2+} at the Li^+ site can be situated at several different distances from the hole trapped at bridging oxygen O4. A hole should be transferred from O4 to the BO_3 ligand where an electron is trapped. The trapped electron screens a hole from the extra positive charge (Mn^{2+} and Li^+) only partially. Hence, one could expect the Coulomb force to impede the hole hopping to the recombination centre. Our kinetic studies revealed the presence of an increased recombination barrier. However, we should not forget that a hole cannot be easily mobilized in $\text{Li}_2\text{B}_4\text{O}_7$ due to the stratified structure of a valence band [9]. The valence band has a narrow sub-band at the top, composed mostly of the orbitals of BO_4 clusters (so, mostly of oxygen 2p states). A hole in the fairly narrow upper sub-band can turn into a small-radius polaron state [41]. This means that hole hopping itself requires a certain amount of activation energy. A similar case was described by the Marcus–Emin–Holstein–Austin–Mott theory in various TiO_2 minerals, where the hole also behaves as a small polaron [42]. In our case, there are non-equivalent states at different hole positions (non-adiabatic case), and also, we expect that Coulomb potential additionally impedes hole hopping.

It is difficult to make exact calculations and to take into account all the factors, such as deformation of valence band by a low-symmetry Coulomb force and so on. So we try a simplified model using a single Boltzmann exponent with some “effective” activation energy to describe hole hopping (the recombination rate contains the Boltzmann factor, see below). As concerns a reciprocal square-root temperature-dependence $T^{-1/2}$, which is present in the Marcus formula, it can be neglected as a “slow” function of temperature within a limited temperature range of each particular TSL peak.

Let us take a look at the activation energy values for hole hopping either in $\text{Li}_2\text{B}_4\text{O}_7$ or in similar materials. The values for TiO_2 given in [42] vary from 0.17–0.25 eV for adiabatic polaron transfer to 0.55–0.62 eV for non-adiabatic cases. Ionic-to-electronic conductivity transition was studied in gold-doped lithium borate glass ($20\text{Li}_2\text{O}\cdot80\text{B}_2\text{O}_3$) [43]. Two activation energies were observed, 1.05 and 0.34 eV. The lower of the two values is related to hopping of small polarons [43]. The mixed polaronic–ionic conductivity was investigated for $\text{Li}_2\text{B}_8\text{O}_{13}$ glasses doped with different amounts of CuO [44]. The temperature of transition from polaronic to ionic conductivity varied from 420 K to approximately 450 K depending on CuO concentrations, and activation energy of ionic conductivity varied from 0.8 to 1.22 eV [44]. The investigations of charge transport in undoped $\text{Li}_2\text{B}_4\text{O}_7$ single crystals and glasses [38] demonstrated high activation energy of conductivity through Li^+ ion hopping (1.22 eV). A lower value (0.71 eV) was found for $\text{Li}_2\text{B}_4\text{O}_7$ glass [38].

We can distinguish now between Li^+ ion hopping and polaron hopping activation energies when considering the results of [45] from our “partial” point of view. Short-living radiation-induced transient optical absorption bands were observed in LiB_3O_5 , $\text{Li}_2\text{B}_4\text{O}_7$, and $\text{Li}_6\text{Gd}(\text{BO}_3)_3$ single crystals, and these bands were connected with polarons [45]. Temperature dependence of the absorption decay kinetics was explained in the frame of a diffusion model as a result of Li hopping activation. However, the authors consider that the induced absorption can decrease not only through the ionic process of diffusion-limited annihilation of lithium vacancies with Li^0 interstitial atoms. The tunnel processes and polaron hopping are not excluded either. The temperature dependences of kinetic parameters of the absorption decay are used to estimate respective activation energies. The results are: 0.54 eV for LiB_3O_5 , 0.42 eV for $\text{Li}_2\text{B}_4\text{O}_7$, and 0.32 eV for $\text{Li}_6\text{Gd}(\text{BO}_3)_3$ single crystals [45]. We see that the activation energies are lower than expected for ionic hopping in these materials, but they suit well for polaron hopping. Probably, the induced transient absorption decay should be connected also with polarons hopping to some recombination centres. As for $\text{Li}_2\text{B}_4\text{O}_7$, two different activation energies are found at the plot (fig. 3b in [45]).

The larger of the two values should be relevant to the ionic process, and the smaller one to polaron hopping. Here we have a good estimation for polaron hopping activation energy in $\text{Li}_2\text{B}_4\text{O}_7$ with the value of 0.42 eV.

As we shall see below, essentially larger values for recombination activation energies were obtained in our kinetic studies for the dosimetric TSL peak (470–510 K) in $\text{Li}_2\text{B}_4\text{O}_7:\text{Mn}$ and for the TSL peak at 525–625 K in case of $\text{Li}_2\text{B}_4\text{O}_7:\text{Mn,Be}$ (Fig. 3). This is what we expected from the suggested model of electron traps.

However, one should take into account several possible positions of a trapped electron relative to a trapped at O4 hole. The closest Li^+ site near Mn^{2+} at the B^{3+} tetrahedral position (just behind O1–O3–O4 oxygen plane of the same tetrahedron, see Fig. 2a) could be too tight for Mn^{2+} due to the deformation of the oxygen tetrahedron containing another Mn^{2+} . If Mn^{2+} ever occurred here at Li^+ position, neither a hole nor an electron would be trapped at room temperature due to very close charge compensation. When Mn^{2+} occurs at the Li^+ position behind the O1–O3–O4 oxygen plane of the B–4O tetrahedron adjacent to that containing Mn^{2+} instead of B^{3+} , both a hole trapping at O4 and an electron trapping at an antibonding BO_3 orbital split off from the bottom of the conduction band would be possible in this complex. Due to the close positions of traps, the recombination would not require hole hopping, and also, a decreased activation energy for recombination is expected. The occupied with a trapped electron antibonding BO_3 orbital is oriented mostly perpendicularly to a BO_3 plane. Thermal activation of the hole to an excited state causes the wave functions of the trapped at O4 hole and the electron to overlap as temperature increases. As a result, the recombination would occur at oxygen O4, with the energy being transferred to Mn^{2+} at the B^{3+} position instead of Mn^{2+} at the Li^+ site. We shall see below that the low-temperature peak (335–345 K) obeys a pure first-order kinetics, so it can be accounted for by the suggested model.

A high-temperature TSL peak (470–510 K) occurs when Mn^{2+} is situated at a more distant Li^+ site after O2 (near a BO_3 plane, see Fig. 2a). There are two such positions, and they are non-equivalent relative to O4 when Mn^{2+} is present instead of B^{3+} in one of two adjacent tetrahedra. Hence, slightly different hole hopping activation energies will be expected for hole transfer to these two non-equivalent positions. As we shall see below, a dosimetric TSL peak (470–510 K) is composed of two very close maxima, so the model accounts for the experimental data. The same is true for the TSL peak at 525–625 K in the case of $\text{Li}_2\text{B}_4\text{O}_7:\text{Mn,Be}$.

Thermoluminescence kinetics

Let us turn to the kinetics data for high-temperature TSL peaks (470–510 K for $\text{Li}_2\text{B}_4\text{O}_7:\text{Mn}$ and 525–625 K

for $\text{Li}_2\text{B}_4\text{O}_7:\text{Mn,Be}$). Decay kinetics measured at each temperature point consists of two exponents, the faster one and the slower one. The time constant of each exponent decreases with the temperature increase. We have already encountered this behaviour in other TLD materials (see, for example, our paper [46]). There should be some closed system of a hole and an electron, with a probability of side recombinations being negligibly low. Such a closed system with bi-exponential decay can be described with two combined linear homogeneous differential equations.

Let us designate the number of stored at O4 holes by N_{ST} and the number of holes thermally released from traps by N_{EX} . W_{T} is the probability of trapped holes to be thermally released, $W_{\text{T}} = W_{\text{T}0} \cdot e^{(-E_{\text{T}}/kT)}$, where $W_{\text{T}0}$ is usually called a frequency factor, E_{T} is thermal release activation energy, and k is the Boltzmann constant. W_{C} is recapturing probability (we do not exclude recapturing to the same trap from where a hole has been released). W_{R} is the recombination probability, and we should take into consideration here the temperature-dependent probability of hole hopping to the recombination centre: $W_{\text{R}} = W_{\text{R}0} \cdot e^{(-E_{\text{R}}/kT)}$, where $W_{\text{R}0}$ is not only a frequency factor but includes also all luminescence probability factors, and E_{R} is recombination activation energy. Actually, it is hole hopping activation energy. As we shall see from the results, E_{R} is larger than the activation energy of polaron hopping (0.42 eV, fig. 3b in [45]). We suppose it to increase due to incompletely screened positive charges of Mn^{2+} and Li^+ . The number of stored holes decreases on the account of thermally released holes and increases due to recapturing released holes:

$$\frac{dN_{\text{ST}}}{dt} = -W_{\text{T}} \cdot N_{\text{ST}} + W_{\text{C}} \cdot N_{\text{EX}}. \quad (1)$$

The number of released from traps holes increases on the account of some more thermally released holes and decreases both due to recapturing and recombination:

$$\frac{dN_{\text{EX}}}{dt} = W_{\text{T}} \cdot N_{\text{ST}} - W_{\text{C}} \cdot N_{\text{EX}} - W_{\text{R}} \cdot N_{\text{EX}}. \quad (2)$$

Luminescence intensity will be a product of recombination probability and the number of released holes: $I_{\text{LUM}} = W_{\text{R}} \cdot N_{\text{EX}}$. The solution of combined equations (1) and (2) is a sum of two exponents: $A_1 \cdot e^{\lambda_1 t} + A_2 \cdot e^{\lambda_2 t}$. The factors λ_1 and λ_2 under the exponents can be determined from the characteristic equation:

$$\lambda^2 + \lambda \cdot (W_{\text{C}} + W_{\text{R}} + W_{\text{T}}) + W_{\text{R}} \cdot W_{\text{T}} = 0.$$

Using Viète theorem, we have:

$$\begin{aligned} \lambda_1 + \lambda_2 &= -(W_{\text{C}} + W_{\text{R}} + W_{\text{T}}) \\ &= -(W_{\text{C}} + W_{\text{R}0} \cdot e^{(-E_{\text{R}}/kT)} + W_{\text{T}0} \cdot e^{(-E_{\text{T}}/kT)}) \end{aligned}$$

and

$$\lambda_1 \cdot \lambda_2 = W_{\text{R}} \cdot W_{\text{T}} = W_{\text{R}0} \cdot W_{\text{T}0} \cdot e^{-(E_{\text{R}} + E_{\text{T}})/kT}.$$

It is more convenient to represent the solution with a sum of two decaying exponents: $A_1 \cdot e^{-t/\tau_1} + A_2 \cdot e^{-t/\tau_2}$, with the decay times $\tau_1 = -1/\lambda_1$ and $\tau_2 = -1/\lambda_2$. From this solution the following equations for the parameters of kinetics can be derived:

$$\ln\left(\frac{1}{\tau_1} \cdot \frac{1}{\tau_2}\right) = \ln(W_{\text{R}0} \cdot W_{\text{T}0}) - \frac{(E_{\text{R}} + E_{\text{T}})}{kT}, \quad (3)$$

$$\frac{1}{\tau_1} + \frac{1}{\tau_2} = (W_{\text{C}} + W_{\text{R}0} \cdot e^{(-E_{\text{R}}/kT)} + W_{\text{T}0} \cdot e^{(-E_{\text{T}}/kT)}). \quad (4)$$

The results of afterglow kinetics measurements were nicely approximated by two exponents at each temperature point. Then the logarithms of products of reciprocal time constants and the sum of reciprocal time constants were plotted against $1/kT$ to obtain kinetics parameters. The results are shown in Fig. 5a for $\text{Li}_2\text{B}_4\text{O}_7:\text{Mn}$ and 5b for $\text{Li}_2\text{B}_4\text{O}_7:\text{Mn,Be}$. The parameters obtained by approximations with functions according to equations (3) and (4) are given in Table 2.

The TL peaks before kinetics measurements and residual after measurements are shown in Fig. 5aa and 5bb for $\text{Li}_2\text{B}_4\text{O}_7:\text{Mn}$ and $\text{Li}_2\text{B}_4\text{O}_7:\text{Mn,Be}$, respectively. The residual after kinetics measurements TL peak (together with the thermal background) was subtracted from the initial one to obtain the “purified” TL peak involved in the measured afterglow. Following the model, this TL peak was digitally simulated, solving the equations by the 4th order Runge–Kutta method with time substituted for temperature (linear heating, $T = T_0 + \beta \cdot t$). A cloud of random values was generated around each parameter value, then the equations were solved for each point in the cloud (Monte-Carlo simulation). The minimal difference between the generated TL peak and the experimental curve was used as a criterion to select the best values for any next step. The difference was calculated only for the growing half of the TL peak (the accuracy of the subtraction of the residual TL peak and thermal background was insufficient for obtaining the falling part of the studied peak undistorted). During the Monte-Carlo calculations, the following restrictions were applied: a sum of activation energies $E_{\text{T}} + E_{\text{R}}$ and a product of frequency factors $W_{\text{R}0} \cdot W_{\text{T}0}$ were fixed (these parameters were taken from kinetics measurements). Variation of the restricted parameters was allowed within the limits of experimental errors.

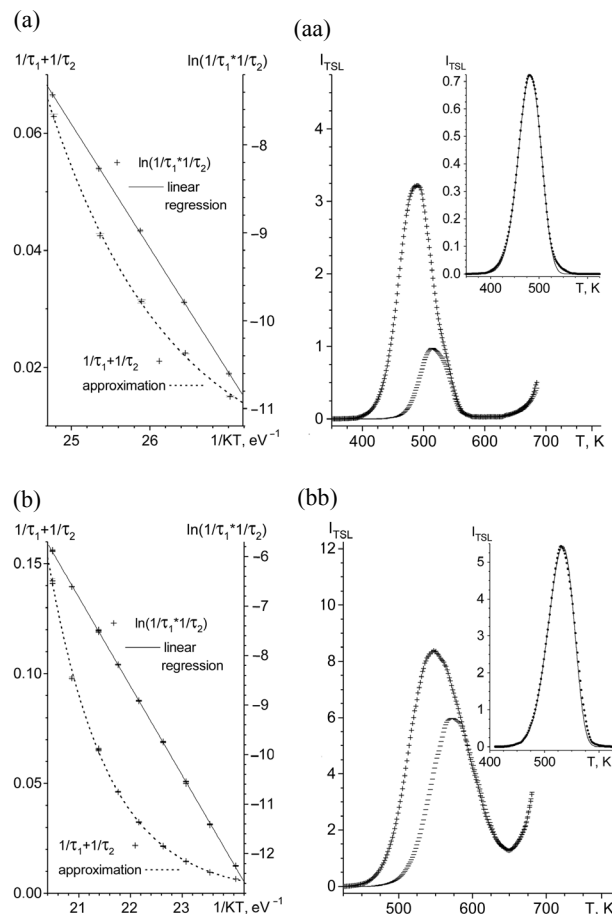


Fig. 5. Kinetics data (a, b) and TSL peak simulation (aa, bb) for $\text{Li}_2\text{B}_4\text{O}_7:\text{Mn}$ (a, aa) and $\text{Li}_2\text{B}_4\text{O}_7:\text{Mn,Be}$ (b, bb). $\ln(1/\tau_1 \cdot 1/\tau_2)$ is plotted as a function of $1/kT$ (see Eq. (3)). Linear regression gives both the sum of activation energies, $E_R + E_T$, and $\ln(W_{R0} \cdot W_{T0})$. The sum of reciprocal decay constants ($1/\tau_1 + 1/\tau_2$) is plotted against $1/kT$. It is approximated by the sum of two exponents (see Eq. (4)), with fixed sum of activation energies and fixed product of pre-exponential factors taken from the linear regression. TSL peaks (aa) and (bb) recorded after kinetics measurement (---) were subtracted from peaks recorded before kinetics measurements (+++). The difference peak was used for computer simulation. It is plotted in the insertions with dots (...), and the simulation result is plotted with a solid line (—).

The simulated TL peaks together with the experimental data (TL peak obtained after subtraction) are plotted in the insertions of Fig. 5. A surprisingly good accuracy of the simulation of TL peaks is worth noting. This indicates the applicability of the suggested kinetic model for the obtained experimental data. The values of kinetics parameters were improved after peak simulation; they are shown in Table 2 together with the initial values used as a starting point for calculations. The improved values occur mostly in the range of experimental errors of parameters initially determined (errors are large, however, for frequency factors W_{R0} and W_{T0} due to the exponential function). Low errors in final (obtained by TSL peak simulation) values are explained by the very large Monte-Carlo flow (1500–2000 points in a cloud). Twenty best results were selected to obtain average values of parameters and their standard deviations.

As mentioned above, the obtained recombination activation energy (E_R) exceeds 1.5–2 times the polaron hopping activation energy of 0.42 eV deduced from [45]. This fact is in accordance with the idea of incomplete screening of positive charges in the vicinity of the recombination centre near Mn^{2+} at the Li^+ position: the hole hopping activation energy is increased due to a repelling Coulomb force.

We tried the same Monte-Carlo calculations procedure for the low-temperature peak in $\text{Li}_2\text{B}_4\text{O}_7:\text{Mn}$ (335–345 K). The result shows a very essential difference for the low-temperature peak compared with the high-temperature one. First, there is no recombination (or hole hopping) activation energy: $E_R = 0$. At the same time, the recombination probability is relatively high ($W_R = 0.15$). Second, the recapturing probability W_C tends to become zero (about 1.4×10^{-16}). Without a recapturing term, the two combined equations become independent ones and describe a “pure” first-order kinetics. The thermal activation energy of the process ($E_T = 0.45$ eV) is lower than in case of the hole release from a trap, and the frequency factor is lower as well ($W_{T0} = 1.14 \times 10^5 \text{ s}^{-1}$).

All these results indicate that we deal with a quasi-intra-centre process, when both a hole and an electron

Table 2. Kinetics parameters obtained from kinetics measurements and TL peak simulation

	$\text{Li}_2\text{B}_4\text{O}_7:\text{Mn}$		$\text{Li}_2\text{B}_4\text{O}_7:\text{Mn,Be}$	
	From kinetics	From TL simulation	From kinetics	From TL simulation
E_T	0.78 ± 0.08 eV	0.7577 ± 0.0006 eV	0.921 ± 0.017 eV	0.9174 ± 0.0022 eV
W_{T0}	$(0.74 \pm 1.41) \times 10^6 \text{ s}^{-1}$	$(1.058 \pm 0.015) \times 10^6 \text{ s}^{-1}$	$(3.22 \pm 1.14) \times 10^6 \text{ s}^{-1}$	$(4.89 \pm 0.23) \times 10^6 \text{ s}^{-1}$
E_R	0.63 ± 0.08 eV	0.6316 ± 0.0008 eV	0.876 ± 0.017 eV	0.8598 ± 0.0021 eV
W_{R0}	$(0.31 \pm 0.57) \times 10^6 \text{ s}^{-1}$	$(0.391 \pm 0.007) \times 10^6 \text{ s}^{-1}$	$(8.27 \pm 2.72) \times 10^6 \text{ s}^{-1}$	$(15.6 \pm 0.6) \times 10^6 \text{ s}^{-1}$
W_C	$(0.72 \pm 3.51) \times 10^{-3} \text{ s}^{-1}$	$(0.466 \pm 0.015) \times 10^{-3} \text{ s}^{-1}$	$(0.08 \pm 0.72) \times 10^{-3} \text{ s}^{-1}$	$(0.045 \pm 0.002) \times 10^{-3} \text{ s}^{-1}$

are captured at a small distance, and thermally activated recombination occurs without transport of charge carriers. This could be expected when the electron is trapped near the Mn^{2+} substituting for Li^+ behind the O1–O3–O4 oxygen plane of the B–4O tetrahedron (adjacent to the tetrahedron with the Mn^{2+} substituting for B^{3+}). The recombination occurs at O4 oxygen (where a hole is captured) when the wave functions of the captured hole and the captured electron become overlapped due to the thermal activation of the hole to an excited state. A more detailed model, however, will require more experimental and computational data.

X-ray-induced absorption and optically stimulated emptying of traps

X-irradiation causes the $\text{Li}_2\text{B}_4\text{O}_7$ -based radiation detectors to acquire absorption bands. The greyish colouring can be seen by the naked eye after doses as large as 10 kGy cm^{-2} or higher are applied.

The normalized reflection spectra of the X-irradiated samples (960 Gy cm^{-2}) are shown in Fig. 6a for $\text{Li}_2\text{B}_4\text{O}_7:\text{Mn}$ and Fig. 6b for $\text{Li}_2\text{B}_4\text{O}_7:\text{Mn,Be}$. The OSL stimulation spectra are shown at the same plots to compare the absorption and stimulation bands. One can see the correlation of X-ray-induced absorption and stimulation bands in the UV region. Both stimulation

and absorption bands are shifted towards longer wavelengths in the case of $\text{Li}_2\text{B}_4\text{O}_7:\text{Mn,Be}$. Also, in this case there is a simpler structure of the absorption band. This could be caused by more complex electronic structures in case of Mn^{2+} at the B^{3+} position compared to the Be^{2+} at the B^{3+} site. At the same time, $\text{Li}_2\text{B}_4\text{O}_7:\text{Mn,Be}$ has an additional narrow stimulation band peaked at 420 nm. We suppose that this additional band is connected with extra high doses (about 10^5 Gy) used for measuring the OSL stimulation spectra. Such high doses cause Mn recharging, and the peculiar stimulation band will appear. This band is absent in the absorption induced by a two orders of magnitude smaller radiation dose. So, this additional sharp band near 420 nm is not appropriate when OSL readout is used for practical doses.

The radiation-induced transient optical absorption bands that are observed in pure $\text{Li}_2\text{B}_4\text{O}_7$ [45] are similar to the absorption bands in the UV region detected in our study for $\text{Li}_2\text{B}_4\text{O}_7:\text{Mn}$ and $\text{Li}_2\text{B}_4\text{O}_7:\text{Mn,Be}$, but with an essential difference in stability: in our case, the radiation-induced absorption bands are stable for months at room temperature. Still, in both cases the radiation-induced absorption bands are connected with holes (or polarons [45]). In both cases, this is an absorption of the O^- centre, where a hole is captured at O4 oxygen. In our case, the hole is stabilized by the Mn^{2+} (or Be^{2+}) substituting for B^{3+} , while in [45] the dynamically displaced Li^+ is supposed to stabilize the hole. Absorption should be connected with electron transition from the deeper valence-band layer to the level where a hole is trapped. The deeper valence-band layer is connected with BO_3 groups and lies about 2–3 eV below the upper valence-band layer [7–9]. The transitions occur from this sub-band to the level with a trapped hole, and the hole is transferred into the deeper sub-band connected with BO_3 groups, where a significant dispersion exists in the band structure [9]. This should cause a hole to acquire certain mobility, resulting in hole transfer to a recombination centre. If this model is true, the cleaning of TL peaks by proper UV radiation should be observed. This effect was observed in our studies, and thus the radiation-induced absorption bands and OSL stimulation spectra were connected with the observed TL peaks.

We tried the irradiation of the excited samples with powerful LEDs emitting quanta exactly in the spectral region of radiation-induced absorption bands. The results are shown in Fig. 7. The low-temperature part of the dosimetric peak is easily cleaned with UV-radiation during 1–2 h, while the maximum at higher temperature survives for longer UV-irradiation times. It is interesting to note that a low-temperature TL peak (335–345 K) studied for $\text{Li}_2\text{B}_4\text{O}_7:\text{Mn,Be}$ was cleaned out during tens of seconds, thus demonstrating much higher sensitivity to UV-irradiation compared to the dosimetric TSL curve area.

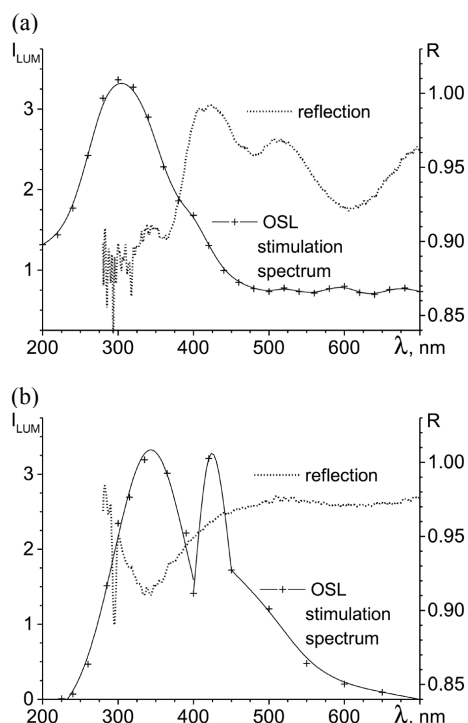


Fig. 6. Normalized reflection spectra (dotted line) after X-irradiation with a dose of 960 Gy cm^{-2} for $\text{Li}_2\text{B}_4\text{O}_7:\text{Mn}$ (a) and $\text{Li}_2\text{B}_4\text{O}_7:\text{Mn,Be}$ (b). OSL stimulation spectra are shown in the same plots (—+—).

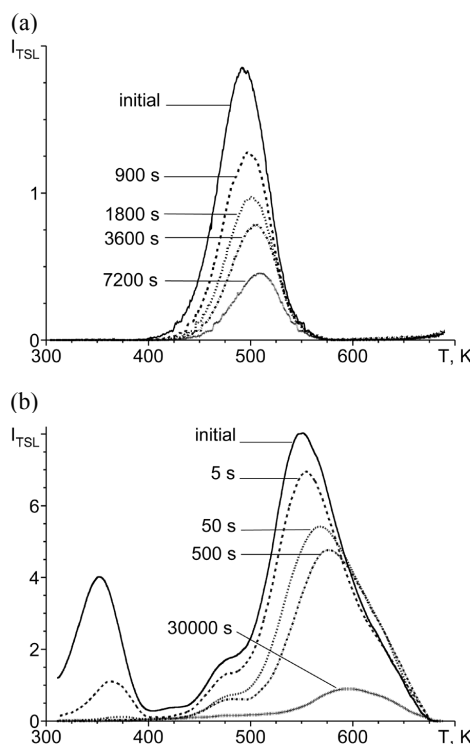


Fig. 7. Optical emptying of traps in $\text{Li}_2\text{B}_4\text{O}_7:\text{Mn}$ (a) and $\text{Li}_2\text{B}_4\text{O}_7:\text{Mn,Be}$ (b). Detectors were irradiated before each run with the same dose: $\text{Li}_2\text{B}_4\text{O}_7:\text{Mn}$ with a dose of 1.5 Gy using a $^{90}\text{Sr}/^{90}\text{Y}$ radiation source, and $\text{Li}_2\text{B}_4\text{O}_7:\text{Mn,Be}$ with a dose of about 0.28 Gy (230 s) using a ^{239}Pu radiation source. $\text{Li}_2\text{B}_4\text{O}_7:\text{Mn}$ samples were pre-heated at 353 K for 30 min before UV-irradiation (365 nm, 25 mW) to remove the low-temperature peak, while $\text{Li}_2\text{B}_4\text{O}_7:\text{Mn,Be}$ were immediately subjected to UV-light (395 nm, 95 mW) and then measured after a small pause. The UV-irradiation times are marked in the plots near the corresponding TSL curves.

The different efficiency of cleaning TL peaks is in good agreement with the model based on different relative positions of hole and electron trapping centres. When Mn^{2+} occurs at the Li^+ position behind the O1–O3–O4 oxygen plane of the B–4O tetrahedron (adjacent to the tetrahedron containing Mn^{2+} instead of B^{3+}), a pronounced fading of the corresponding TL peak (335–345 K) is observed at room temperature, and also, a very fast cleaning of this peak occurs when a hole is excited by UV-irradiation. Recombination is activated when the hole is either thermally or optically promoted to an excited state, with the wave functions of the excited hole and the trapped electron being overlapped. When Mn^{2+} is located at the Li^+ site after O2 (near the BO_3 plane), we have a “dosimetric” electron trap being cleaned due to its recombination with a hole delivered either by thermal activation or by optical stimulation. The electron traps of this kind are situated at two different distances. The more distant is Mn^{2+} at the Li^+ position from the captured at O4 hole, the higher is the

TSL maximum and the more time is required to clean it optically. This indicates that optically stimulated release of a hole from a trap is insufficient for effective hole transport to the recombination centre. A hole still needs an additional energy to overcome a hopping barrier. Hence, a thermo-optical stimulation should be studied for $\text{Li}_2\text{B}_4\text{O}_7:\text{Mn}$, with optical stimulation and simultaneous heating to temperatures close to 370 K to provide hole hopping activation.

CONCLUSIONS

The studied ceramic radiation detectors $\text{Li}_2\text{B}_4\text{O}_7:\text{Mn}$ and $\text{Li}_2\text{B}_4\text{O}_7:\text{Mn,Be}$ contain mostly polycrystalline lithium tetraborate, with the amount of glass phase being negligible. The incorporation of Mn into the lattice structure of $\text{Li}_2\text{B}_4\text{O}_7$ is possible both at Li^+ sites and at B^{3+} tetrahedral positions. The latter is possible due to the adaptation of the size of the oxygen tetrahedron by the displacement of bridging oxygen connecting two adjacent BO_4 tetrahedra. Two different luminescence bands observed for different TSL peaks [18] belong to these two different Mn^{2+} centres.

The different temperature dependences of the observed EPR signals belonging to Mn^{2+} helped to reveal two types of Mn^{2+} centres with different local surroundings. To prove the presence of Mn^{2+} at B^{3+} tetrahedral positions, an analogy with $\text{BeO}:\text{Mn}^{2+}$ [27] is useful because HFS splitting values for Mn^{2+} in BeO and in $\text{Li}_2\text{B}_4\text{O}_7$ are similar. EPR studies of Mn^{2+} in $\text{Li}_2\text{B}_4\text{O}_7:\text{Mn}$ and $\text{Li}_2\text{B}_4\text{O}_7:\text{Mn,Be}$ showed the suppression of Mn^{2+} at the B^{3+} position in the presence of Be^{2+} , and also an increase of Mn^{2+} clusterization, in which Mn^{2+} ions substituting for Li^+ were involved, instead of increasing the number of isolated Mn_{Li} centres.

A hole is captured at O4 (the bridging oxygen of two adjacent BO_4 tetrahedra) when one of two adjacent tetrahedra contains Mn^{2+} instead of B^{3+} . The red luminescence of Mn^{2+} at the B^{3+} tetrahedral position is actually a thermally activated quasi-intra-centre recombination. It occurs when the captured at O4 hole is recombined with an electron captured at a closely situated electron trap. This trap is caused by Mn^{2+} at the Li^+ site behind the O1–O3–O4 oxygen plane of the B–4O tetrahedron adjacent to the tetrahedron containing Mn^{2+} instead of B^{3+} . The recombination is activated when the hole is thermally promoted to an excited state, with the wave functions of the excited hole and the trapped electron being overlapped. The orange luminescence of Mn^{2+} at the Li^+ position occurs when a hole (released from O4 in the case of TSL) recombines with an electron captured near Mn^{2+} situated at a more distant Li^+ position from O4. Two slightly different Mn^{2+} positions are involved, both situated at the Li^+ site after oxygen

O₂ (near a BO₃ plane, see Fig. 2a). The electronic trapping level is connected with an antibonding BO₃ orbital split off from the bottom of the conduction band due to the extra positive charge of Mn²⁺ at the Li⁺ position. Both luminescence bands (red and orange) can be attributed to ⁴T₁–⁶A₁ radiative transitions of Mn²⁺ in two different distorted tetrahedral environments.

The basic (dosimetric) TSL peak in $\text{Li}_2\text{B}_4\text{O}_7:\text{Mn}$ is connected with the release of holes and occurs at 470–510 K. In the case of $\text{Li}_2\text{B}_4\text{O}_7:\text{Mn,Be}$, this peak is essentially suppressed in favour of a new intensive group of maxima created in the range of 525–625 K. Compared to $\text{Li}_2\text{B}_4\text{O}_7:\text{Mn}$, a deeper hole trap is formed in $\text{Li}_2\text{B}_4\text{O}_7:\text{Mn,Be}$ at O4 when Be²⁺ is substituting for B³⁺. Be²⁺ occupies the positions of tetrahedral B³⁺ much more efficiently than Mn²⁺. This causes the amount of Mn²⁺ at the position of B³⁺ to decrease, and the amount of Mn²⁺ at the position of Li⁺ to increase. This fact is supported also by comparative EPR studies of $\text{Li}_2\text{B}_4\text{O}_7:\text{Mn}$ and $\text{Li}_2\text{B}_4\text{O}_7:\text{Mn,Be}$.

The TSL kinetics studied for either material, $\text{Li}_2\text{B}_4\text{O}_7:\text{Mn}$ or $\text{Li}_2\text{B}_4\text{O}_7:\text{Mn,Be}$, shows both a bi-exponential decay at each temperature point. To account for the observed kinetics data, a simple quasi-intra-centre model is suggested. The model neglects side recombinations and takes into consideration a hole hopping activation barrier. The dosimetric TL peak was digitally simulated on the basis of the suggested model, and the simulation results almost coincide with the experimental data. Kinetics parameters were determined in the frame of the suggested model (see Table 2). The results demonstrated an increased barrier for the released hole hopping towards the recombination centre. This is in accordance with the suggested structural model: the captured near Mn_{Li} electron does not provide a complete screening of the Mn²⁺ positive charge, so an additional Coulomb repelling force is expected, which increases the “normal” polaron hopping activation energy.

The low-temperature TSL peak (335–345 K) with the red Mn²⁺ luminescence shows a “pure” first-order kinetics and occurs without hole hopping and without recapturing. The activation energy ($E_{\text{T}} = 0.45 \text{ eV}$) is lower than in the case of hole release. The close Mn_B–Mn_{Li} pair is responsible for this peak, with a hole trapped at O4 bridging oxygen and an electron trapped near Mn²⁺ at the Li⁺ site behind the O1–O3–O4 oxygen plane of the closest B–4O tetrahedron (adjacent to the one containing Mn²⁺ instead of B³⁺). The trapped electron occupies an antibonding BO₃ orbital split off from the bottom of the conduction band. The wave functions of the electron and the captured at O4 hole overlap each other with a temperature increase, and the recombination occurs at O4, with the energy being transferred to Mn²⁺ at the B³⁺ position yielding the red luminescence band.

The radiation-induced absorption bands and OSL stimulation spectra were studied both for $\text{Li}_2\text{B}_4\text{O}_7:\text{Mn}$ and $\text{Li}_2\text{B}_4\text{O}_7:\text{Mn,Be}$. The absorption bands in the UV region correlated with OSL stimulation spectra. The OSL stimulation maximum was shifted towards longer wavelengths by 30–40 nm in the case of $\text{Li}_2\text{B}_4\text{O}_7:\text{Mn,Be}$. The optical emptying of traps was observed at stimulation with powerful LEDs at corresponding wavelengths. The efficient cleaning of dosimetric TSL peaks requires additional energy for hole hopping activation. The obtained results will be useful for practical application of $\text{Li}_2\text{B}_4\text{O}_7:\text{Mn}$ and $\text{Li}_2\text{B}_4\text{O}_7:\text{Mn,Be}$ in dosimetry with OSL readout.

ACKNOWLEDGEMENTS

We acknowledge the financial support from the Estonian Science Foundation (grant 7623), from targeted financing project SF0180089s08 of the Ministry of Education and Research of Estonia, and from the Centre of Excellence HIGHTECHMAT (project SLOKT117T). We are grateful to Ivar Jaek and Valery Vasilchenko for OSL spectra measurements and fruitful discussions and to Nina Melnikova for the TL data treatment.

REFERENCES

- El-Faramawy, N. A., Göksu, H. Y., and Panzer, W. Thermoluminescence dosimetric properties of a new thin beta detector (LiF:Mg, Cu, P; GR-200F) in comparison with highly sensitive Al₂O₃:C beta dosimeters. *J. Radiol. Prot.*, 2004, **24**, 273–282.
- Mobit, P., Agyingi, E., and Sandison, G. Comparison of the energy-response factor of LiF and Al₂O₃ in radiotherapy beams. *Radiat. Prot. Dosim.*, 2006, **119**, 497–499.
- Maia, A. F. and Caldas, L. V. E. Response of TL materials to diagnostic radiology X radiation beams. *Appl. Radiat. Isot.*, 2010, **68**, 780–783.
- Selvam, T. P. and Keshavkumar, B. Monte Carlo investigation of energy response of various detector materials in ¹²⁵I and ¹⁶⁹Yb brachytherapy dosimetry. *J. Appl. Clin. Med. Phys.*, 2010, **11**(4), 70–82.
- Gorelik, V. S., Vdovin, A. V., and Moiseenko, V. N. Raman and hyper-Rayleigh scattering in lithium tetraborate crystals. *J. Russ. Laser Res.*, 2003, **24**, 553–605.
- Kuznetsov, A. Yu., Krushalov, A. V., Ogorodnikov, I. N., Sobolev, A. B., and Isaenko, L. I. Electronic structure of lithium tetraborate $\text{Li}_2\text{B}_4\text{O}_7$ crystals. Cluster calculations and x-ray photoelectron spectroscopy. *Phys. Solid State*, 1999, **41**, 48–50.
- Maslyuk, V. V., Islam, M. M., and Bredow, T. Electronic properties of compounds of the Li_2O – B_2O_3 system. *Phys. Rev. B*, 2005, **72**, 125101 (9 pp).

8. Islam, M. M., Maslyuk, V. V., Bredow, T., and Minot, C. Structural and electronic properties of $\text{Li}_2\text{B}_4\text{O}_7$. *J. Phys. Chem. B*, 2005, **109**, 13597–13604.
9. Adamiv, V. T., Burak, Ya. V., Wooten, D. J., McClory, J., Petrosky, J., Ketsman, I., Xiao, J., Losovyj, Ya. B., and Dowben, P. A. The electronic structure and secondary pyroelectric properties of lithium tetraborate. *Materials*, 2010, **3**, 4550–4579.
10. Wooten, D., Ketsman, I., Xiao, J., Losovyj, Ya. B., Petrosky, J., McClory, J., Burak, Ya. V., Adamiv, V. T., Brown, J. M., and Dowben, P. A. The electronic structure of $\text{Li}_2\text{B}_4\text{O}_7(110)$ and $\text{Li}_2\text{B}_4\text{O}_7(100)$. *Eur. Phys. J. Appl. Phys.*, 2010, **52**, 31601 (8 pp).
11. Swinney, M. W., McClory, J. W., Petrosky, J. C., Yang, Sh., Brant, A. T., Adamiv, V. T., Burak, Ya. V., Dowben, P. A., and Halliburton, L. E. Identification of electron and hole traps in lithium tetraborate ($\text{Li}_2\text{B}_4\text{O}_7$) crystals: oxygen vacancies and lithium vacancies. *J. Appl. Phys.*, 2010, **107**, 113715 (9 pp).
12. Corradi, G., Watterich, A., Polgár, K., Nagirnyi, V., Hofstaetter, A., Rakitina, L. G., and Meyer, M. EPR of Cu^{2+} in lithium tetraborate single crystals. *Phys. Status Solidi (C)*, 2007, **4**, 1276–1279.
13. Corradi, G., Nagirnyi, V., Kotlov, A., Watterich, A., Kirm, M., Polgár, K., Hofstaetter, A., and Meyer, M. Investigation of Cu-doped $\text{Li}_2\text{B}_4\text{O}_7$ single crystals by electron paramagnetic resonance and time-resolved optical spectroscopy. *J. Phys. Condens. Mat.*, 2008, **20**, 025216 (9 pp).
14. Corradi, G., Nagirnyi, V., Watterich, A., Kotlov, A., and Polgár, K. Different incorporation of Cu^+ and Cu^{2+} in lithium tetraborate single crystals. *J. Phys. Conf. Ser.*, 2010, **249**, 012008 (6 pp).
15. Podgórska, D., Kaczmarek, S. M., Drozdowski, W., Wabia, M., Kwaśny, M., Warchał, S., and Rizak, V. M. Charging processes of Mn ions in $\text{Li}_2\text{B}_4\text{O}_7:\text{Mn}$ single crystal and glass samples under the influence of γ -irradiation and annealing. *Molekul. Phys. Rep.*, 2004, **39**, 199–222.
16. Kelemen, A., Ignatovych, M., Holovey, V., Vidoczy, T., and Baranyai, P. Effect of irradiation on photoluminescence and optical absorption spectra of $\text{Li}_2\text{B}_4\text{O}_7:\text{Mn}$ and $\text{Li}_2\text{B}_4\text{O}_7:\text{Ag}$ single crystals. *Radiat. Phys. Chem.*, 2007, **76**, 1531–1534.
17. Podgórska, D., Kaczmarek, S.M., Drozdowski, W., Berkowski, M., and Worsztynowicz, A. Growth and optical properties of $\text{Li}_2\text{B}_4\text{O}_7$ single crystals pure and doped with Yb, Co and Mn ions for nonlinear applications. *Acta Phys. Pol. A*, 2005, **107**, 507–518.
18. Holovey, V. M., Popovich, K. P., Goyer, D. B., Krasylnets, V. M., and Gomonnai, A. V. Spectral dependences of thermally stimulated luminescence and X-ray luminescence of single-crystalline and glassy $\text{Li}_2\text{B}_4\text{O}_7:\text{Mn}$. *Radiat. Eff. Defect. Solid*, 2011, **166**, 522–528.
19. Danilkin, M., Jaek, I., Kerikmäe, M., Lust, A., Mändar, H., Pung, L., Ratas, A., Seeman, V., Klimonsky, S., and Kuznetsov, V. Storage mechanism and OSL-readout possibility of $\text{Li}_2\text{B}_4\text{O}_7:\text{Mn}$ (TLD-800). *Radiat. Meas.*, 2010, **45**, 562–565.
20. Kerikmäe, M., Danilkin, M., and Lust, A. $\text{Li}_2\text{B}_4\text{O}_7$ based transparent tissue-equivalent radiation detector for thermally or optically stimulated luminescence dosimetry and fabricating method thereof. Patent application of the University of Tartu. Priority date: 29.01.2010. Intern. Public. No. WO 2011/091803 A1. Estonian applic. No.: EE201000011, PCT applic.: PCT/EE2010/000002. Status: pending.
21. Sennova, N., Bubnova, R., Shepelev, Yu., Filatov, S., and Yakovleva, O. $\text{Li}_2\text{B}_4\text{O}_7$ crystal structure in anharmonic approximation at 20, 200, 400 and 500°C. *J. Alloy. Compd.*, 2007, **428**, 290–296.
22. Ozawa, T. C. and Kang, S. J. Balls & Sticks: easy-to-use structure visualization and animation program. *J. Appl. Cryst.*, 2004, **37**, 679.
23. Abrahams, S. C., Bernstein, J. L., Gibart, P., Robbins, M., and Sherwood, R. C. Manganese diborate: crystal structure, magnetization, and thermal extinction dependence. *J. Chem. Phys.*, 1974, **60**, 1899–1905.
24. Sadanaga, R., Nishimura, T., and Watanabe, T. The structure of jimboite, $\text{Mn}_3(\text{BO}_3)_2$ and relationship with the structure of kotoite. *Mineral. J.*, 1965, **4**, 380–388.
25. Norrestam, R., Kritikos, M., and Sjödin, A. Manganese(II,III) oxyborate, Mn_2OBO_3 : a distorted homometallic warwickite – synthesis, crystal structure, band calculations, and magnetic susceptibility. *J. Solid State Chem.*, 1995, **114**, 311–316.
26. Smith, D. K., Cline, C. F., and Austerman, S. B. The crystal structure of β -beryllia. *Acta Cryst.*, 1965, **18**, 393–397.
27. Milsch, B. and Kerbe, F. EPR of chromium and manganese ions in beryllium oxide ceramics. *Phys. Status Solidi (A)*, 1987, **103**, K141–K144.
28. Holovey, V. M., Sidey, V. I., Lyamayev, V. I., and Birov, M. M. Influence of different annealing conditions on the luminescent properties of $\text{Li}_2\text{B}_4\text{O}_7:\text{Mn}$ single crystals. *J. Phys. Chem. Solids*, 2007, **68**, 1305–1310.
29. Biernacki, S., Kutrowski, M., Karczewski, G., Wojtowicz, T., and Kossut, J. Temperature variation of the Mn^{2+} luminescence spectra in $\text{Cd}_{1-x}\text{Mn}_x\text{Te}$ crystals. *Semicond. Sci. Technol.*, 1996, **11**, 48–54.
30. Duan, C. J., Delsing, A. C. A., and Hintzen, H. T. Photoluminescence properties of novel red-emitting Mn^{2+} -activated MZnOS ($\text{M} = \text{Ca}, \text{Ba}$) phosphors. *Chem. Mater.*, 2009, **21**, 1010–1016.
31. Griscom, D. L. and Griscom, L. E. Paramagnetic resonance of Mn^{2+} in glasses and compounds of the lithium borate system. *J. Chem. Phys.*, 1967, **47**, 2711–2722.
32. Ramana, M. V., Kumar, K. S., Rahman, S., Babu, D. S., Sathyaranayanan, S. G., and Sastry, G. S. Electron paramagnetic resonance study of Mn^{2+} , Cu^{2+} and VO^{2+} in $\text{Li}_2\text{O}-\text{Na}_2\text{O}-\text{B}_2\text{O}_3$ glasses. *J. Mater. Sci. Lett.*, 1989, **8**, 1471–1473.
33. Chakradhar, S. R. P., Sivaramaiah, G., Rao, L. J., and Gopal, N. O. EPR and optical investigations of manganese ions in alkali lead tetraborate glasses. *Spectrochim. Acta A-M*, 2005, **62**, 761–768.
34. Ardelean, I., Peteanu, M., Mureşan, N., Ioncu, V., and Ciocas-Delille, F. EPR investigation of manganese ions in $70\text{TeO}_2\text{-}25\text{B}_2\text{O}_3\text{-}5\text{MO}$ ($\text{MO} \Rightarrow \text{SrO}$ or SrF_2) glass matrices. *J. Optoelectron. Adv. M.*, 2005, **7**, 2661–2666.
35. Chakradhar, R. P. S., Yasoda, B., Rao, J. L., and Gopal, N. O. EPR and optical studies of Mn^{2+} ions in

- $\text{Li}_2\text{O}-\text{Na}_2\text{O}-\text{B}_2\text{O}_3$ glasses – an evidence of mixed alkali effect. *J. Non-cryst. Solids*, 2007, **353**, 2355–2362.
36. Padlyak, B. V., Wojtowicz, W., Adamiv, V. T., Burak, Ya. V., and Teslyuk, I. M. EPR spectroscopy of the Mn^{2+} and Cu^{2+} centres in lithium and potassium–lithium tetraborate glasses. *Acta Phys. Pol. A*, 2010, **117**, 122–125.
37. Shkrob, I. A., Tadjikov, B. M., and Trifunac, A. D. Magnetic resonance studies on radiation-induced point defects in mixed oxide glasses. I. Spin centers in B_2O_3 and alkali borate glasses. *J. Non-cryst. Solids*, 2000, **262**, 6–34.
38. Rizak, I. M., Rizak, V. M., Baisa, N. D., Bilanich, V. S., Boguslavskii, M. V., Stefanovich, S. Yu., and Golovoi, V. M. Charge transport in $\text{Li}_2\text{B}_4\text{O}_7$ in single crystal and glassy states. *Crystallogr. Rep.*, 2003, **48**, 676–681.
39. Burak, Ya. V., Padlyak, B. V., and Shevel, V. M. Neutron-induced defects in the lithium tetraborate single crystals. *Radiat. Eff. Defect. S.*, 2002, **157**, 1101–1109.
40. Lian, J. C., Finazzi, E., Di Valentin, C., Risso, T., Gao, H.-J., Pacchioni, G., and Freund, H.-J. Li atoms deposited on single crystalline $\text{MgO}(0\ 0\ 1)$ surface. A combined experimental and theoretical study. *Chem. Phys. Lett.*, 2008, **450**, 308–311.
41. Ogorodnikov, I. N., Pustovarov, V. A., Kruzhakov, A. V., Isaenko, L. I., Kirm, M., and Zimmerer, G. Self-trapped excitons in LiB_3O_5 and $\text{Li}_2\text{B}_4\text{O}_7$ lithium borates: time-resolved low-temperature luminescence VUV spectroscopy. *Phys. Solid State*, 2000, **42**, 464–472.
42. Deskins, N. A. and Dupuis, M. Intrinsic hole migration rates in TiO_2 from density functional theory. *J. Phys. Chem. C*, 2009, **113**, 346–358.
43. Jain, H., Issa, A., Anavekar, R. V., Böhmer, R., Kanert, O., and Küchler, R. Ionic-to-electronic conductivity transition in an oxide glass doped with gold. *Appl. Phys. Lett.*, 2009, **95**, 142908 (3 pp).
44. Khalil, M. M. I. Mixed polaronic-ionic conduction in lithium borate glasses and glass-ceramics containing copper oxide. *Appl. Phys. A-Mater.*, 2007, **86**, 505–514.
45. Ogorodnikov, I. N., Poryvay, N. E., and Pustovarov, V. A. Radiation effects and defects in lithium borate crystals. *IOP Conf. Ser.: MSE*, 2010, **15**, 012016 (8 pp).
46. Danilkin, M., Lust, A., Ratas, A., Seeman, V., and Kerikmäe, M. Afterglow kinetics and storage mechanism in $\text{CaF}_2:\text{Mn}$ (TLD-400). *Radiat. Meas.*, 2008, **43**, 300–302.

$\text{Li}_2\text{B}_4\text{O}_7:\text{Mn}$ dosimeetriliseks kasutamiseks: haardenivoode ja mehhanismid

Arno Ratas, Mikhail Danilkin, Mihkel Kerikmäe, Aime Lust, Hugo Mändar,
Viktor Seeman ja Georg Slavin

Töös uuriti haardenivoode struktuuri ja termoluminestsensi mehhismi $\text{Li}_2\text{B}_4\text{O}_7:\text{Mn}$ ning $\text{Li}_2\text{B}_4\text{O}_7:\text{Mn},\text{Be}$ kiirgusdetektoritel. Võrreldi nende kiirgusdetektorite termoluminestsensi kõveraid, luminestsentskineetikat, kiirgusindutseeritud neeldumisribasid, optiliselt stimuleeritud luminestsensi (OSL) stimuleerimise spektreid ja EPR-spektreid. Röntgenstruktuuralüüs abil uuriti kristallvõre erisusi. Materjal on põhiliselt polükristalliline liitiumtetraboraat tühise hulga klaasitaolise faasiga. Saadud andmed koos kirjanduses tooduga võimaldavad kirjeldada haardenivoode ja termoluminestsensi mehhismi. Dosimeetrilised maksimumid on seotud aukude vabanemisega. Luminestsents toimub Li^{+} -i asendavas Mn^{2+} -is. Auk haaratakse tetraeedrilist B^{3+} -i asendava Mn^{2+} -i (või Be^{2+} -i) lähedasel sildhapnikul. Esineb kaht tüüpi luminestsentsi- ja EPR-spektreid. Punane luminestsents B^{3+} -i asendavas Mn^{2+} -is toimub, kui sildhapnikul haardunud auk rekombineerub lähdelt haaratud elektroniga. Rekombinatsioon toimub elektroni ja augu laineefunktsioonide kattumise töttu peale augu termilikat aktiveerimist. Oranž luminestsents tekib Li^{+} -i asendavas Mn^{2+} -is, kui sildhapnikult vabanenud auk rekombineerub Mn^{2+} -i lähdal haardunud elektroniga. Mõlemad luminestsentsribad võib omistada $\text{Mn}^{2+}\text{T}_1^{-6}\text{A}_1$ kiirguslikele üleminekutele. On arutletud Mn^{2+} -i ja ümbritseva hapniku vahelise interaktsiooni mõjust nii Mn^{2+} -i luminestsentsentritele kui ka EPR-spektri peen- ning ülipoenstruktuurile.

EPR-spektrid näitavad kaht tüüpi Mn^{2+} -i tsentrite olemasolu. B^{3+} -i asendava Mn^{2+} -i EPR-joonte intensiivsus tõuseb madalal temperatuuril. Vedela lämmastiku temperatuuril mõõdetud EPR-spektrid annavad võimaluse määratada ülipoenstruktuuri lõhenemise suurust, mis on sarnane kirjanduses toodud suurusega Mn^{2+} -i jaoks tetraeedrilises BeO -s. See näitab, et vaadeldud Mn^{2+} asendab B^{3+} -i tetraeedrilises ümbruses liitiumtetraboraadis.

Nii $\text{Li}_2\text{B}_4\text{O}_7:\text{Mn}$ kui ka $\text{Li}_2\text{B}_4\text{O}_7:\text{Mn},\text{Be}$ luminestsentsi kustumise kineetika on bi-eksponentiaalne igas temperatuuri punktis. Arvutuste tegemiseks on välja pakutud lihtne kineetika mudel, mis kirjeldab eksperimentaalseid andmeid suure täpsusega. Kineetilised mõõtmised näitavad, et augu hüppamise aktivatsiooni energia rekombinatsiooni tsentriile on 1,5–2 korda suurem kui standardne augu liikumise energieetiline barjäär. Lisaaktivatsiooni energia on seotud mittetäielikult varjestatud Mn^{2+} -i positivse laenguga (kus Li^{+} on asendunud Mn^{2+} -iga).

Uuriti ka kiirgusest tingitud neeldumisribasid ja OSL-i stimulatsioonispektritega. OSL-i stimulatsioonispektor on nihkunud 30–40 nm pikemate laine-pikkuste poole $\text{Li}_2\text{B}_4\text{O}_7:\text{Mn},\text{Be}$ korral. Andmed haardenivoode tühjendamise kohta optilise stimuleerimisega näitavad võimalust kasutada $\text{Li}_2\text{B}_4\text{O}_7:\text{Mn}$ ja $\text{Li}_2\text{B}_4\text{O}_7:\text{Mn},\text{Be}$ detektoreid optilise stimuleerimisega lugemise süsteemides.